

Modified LCC Compensation and Magnetic Integration for Inductive Power Transfer

Xinlin Wang^{1b}, *Graduate Student Member, IEEE*, Rong He^{1b}, *Graduate Student Member, IEEE*,
Haoyu Wang^{1b}, *Senior Member, IEEE*, Junrui Liang^{1b}, *Senior Member, IEEE*,
and Minfan Fu^{1b}, *Senior Member, IEEE*

Abstract—An LCC–LCC compensated inductive power transfer (IPT) system has been widely used for the mid- or high-power applications. When dual active bridges (DABs) are used, the famous triple phase shift (TPS) modulation cannot maximize the coupler efficiency when considering the zero-voltage switching (ZVS). A modified LCC compensation is proposed by replacing the input inductor with a transformer. It is able to maintain the benefits of original compensation and dramatically extend the ZVS range, which effectively addresses the conflict between tank efficiency and ZVS. To have a low-profile design, a planar transformer is proposed to be integrated with the coupler, and the winding turn number is used for circuit parameter design. Finally, a 100-W prototype system is implemented based on the modified compensation and magnetic integration solution. In a wide loading and coupling range, the achieved efficiency would be stable within [91.0%, 93.4%]. Compared with the original system, the efficiency improvement at light load condition is 3.7%.

Index Terms—Inductive power transfer (IPT), LCC compensation, magnetic integration, triple phase shift (TPS) modulation.

I. INTRODUCTION

THE inductive power transfer (IPT) is promising for the noncontact charging of movable devices, such as consumer electronics, moving robots, and electric vehicles [1], [2], [3]. Through a basic coupler, the power is delivered from a transmitter (TX) to a receiver (RX), and the transfer efficiency is proportional to the coupling coefficient. To ensure sufficient coupling, a practical IPT system needs to fully consider the size constrains to customize or optimize the coupler [4]. When pursuing high spatial freedom, the multicoil coupler is usually needed with flux modulation capability [5], and such a design logic shows a clear tradeoff design consideration between the

system complexity and moving freedom [6], [7], [8]. In the past few years, the diversity of the inductive coupler dramatically reflects the potentials of the wireless charging systems.

A well-designed coupler itself is not able to ensure efficient power transfer. The compensations are needed to offer an acceptable interface for the front-end inverter or down-stream rectifier. In the early research, only two more capacitors are added to form the basic compensations [9]. The objective is to eliminate the circulation energy and help the RX get a maximized output [10]. An in-depth study of basic compensations helps explore their load-independent output capability. For example, the SS compensation would achieve constant output voltage by sacrificing the zero phase operation (ZPA) [11]. High-order compensation could be synthesized to achieve several attractive features simultaneously, such as the LCC-S compensation [12] and LCC–LCC compensation [13], [14]. The LCC–LCC compensation is attractive due to its constant output current, and this topology has been accepted by the EV charging standard. When compensation inductors are added, it is beneficial to integrate the additional inductors with the planar coupler to have a low-profile design [15], [16]. However, the exciting magnetic integration usually has to analyze the complicated coupling and try to minimize the negative effects.

Besides the magnetic integration, another challenging issue is to develop the modulation approach for an LCC–LCC compensated system. The dual active bridge (DAB) topology is widely used due to its simplicity and ample modulation options, such as pulse density modulation (PDM) [17], pulse frequency modulation (PFM) [18], and phase shift modulation (PSM) [19]. Among these options, PDM allows for precise energy injection into the resonant tank by controlling pulse density. However, it has associated drawbacks such as interharmonics, ac current fluctuations, and increased output ripples. PFM is advantageous for enhancing system output power, but its sensitivity to resonant frequency can lead to the loss of ZPA operation. In comparison to PDM and PFM, PSM is frequently used in various power conversion scenarios. In [20], the dual-phase shift (DPS) modulation is used to regulate the output. However, this approach has limited control variables, resulting in hard switching issues. Introducing triple phase shift (TPS) modulation using the phase between the TX and RX bridge converters allows for soft switching, but it introduces a significant amount of reactive power during

Manuscript received 31 March 2023; revised 22 June 2023 and 1 August 2023; accepted 9 August 2023. Date of publication 15 August 2023; date of current version 5 February 2024. This work was supported by the National Natural Science Foundation of China under Grant 52007120. Recommended for publication by Associate Editor Yi Tang. (*Corresponding author: Minfan Fu.*)

Xinlin Wang is with the School of Information Science and Technology, ShanghaiTech University, Shanghai 201210, China, also with the Shanghai Advanced Research Institute, Shanghai 201210, China, and also with the University of Chinese Academy of Sciences, Beijing 101408, China.

Rong He, Haoyu Wang, Junrui Liang, and Minfan Fu are with the School of Information Science and Technology, Shanghai 201210, China, and also with the Shanghai Engineering Research Center of Energy Efficient and Custom AI IC, Shanghai 201210, China (e-mail: fumf@shanghaitech.edu.cn).

Color versions of one or more figures in this article are available at <https://doi.org/10.1109/JESTPE.2023.3305476>.

Digital Object Identifier 10.1109/JESTPE.2023.3305476

2168-6777 © 2023 IEEE. Personal use is permitted, but republication/redistribution requires IEEE permission.
See <https://www.ieee.org/publications/rights/index.html> for more information.

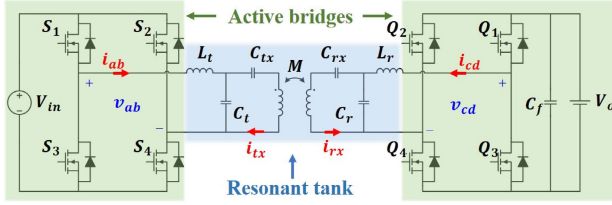


Fig. 1. Classical IPT system using DABs.

coupling and loading variations [21], [22], [23]. In addition, frequency is included in [24] to form a four-degree-of-freedom control strategy to achieve multiple objectives. However, this control scheme becomes overly complex and sacrifices the original benefits of a fixed frequency system, such as independent resonance with coupling and load-independent output current [14]. Therefore, it is advantageous to develop a comprehensive solution that takes into account the characteristics of compensation, magnetic design, and modulation approaches to create a simple and high-performance system.

This article would modify the original LCC compensation and develop the magnetic integration solution for the new system. The operation point of the proposed low-profile design is closer to the global peak efficiency for the resonant tank when considering the varied power demands and zero-voltage switching (ZVS) requirements. When the TPS modulation is used, the limitation of the original LCC compensation is discussed, which shows the global peak efficiency cannot be achieved due to the ZVS operation. The compensation is modified by replacing the input inductor by a loosely coupled transformer. The proposed transformer is easily integrated with the planar coil for a low-profile design. An interleaving winding solution is proposed for the transformer design, and the turn number is freely tuned to meet the requirements of the compensation. The modified LCC compensation would keep all the merits of the original one and help fully explore the benefits of the TPS modulation.

II. DAB-BASED IPT SYSTEM

A. Steady-State Characteristic

A symmetrical DAB-based IPT system is shown in Fig. 1. The system includes a voltage source V_{in} , an RX-side battery (equivalent to a voltage source V_o), and two full-bridge converters. A pair of coils form the inductive coupler, i.e., L_{tx} and L_{rx} , and the mutual inductance is M . The famous LCC-LCC compensation is applied to form the middle resonant tank [25]. L_t , C_t , and C_{tx} are the TX-side compensation components, and L_r , C_r , and C_{rx} are added for the RX side. Given the angular switching frequency ω , the resonance condition is ensured by

$$\begin{cases} \omega L_t - \frac{1}{\omega C_t} = 0 \\ \omega L_{tx} - \frac{1}{\omega C_{tx}} = \omega L_t \\ \omega L_r - \frac{1}{\omega C_r} = 0 \\ \omega L_{rx} - \frac{1}{\omega C_{rx}} = \omega L_r. \end{cases} \quad (1)$$

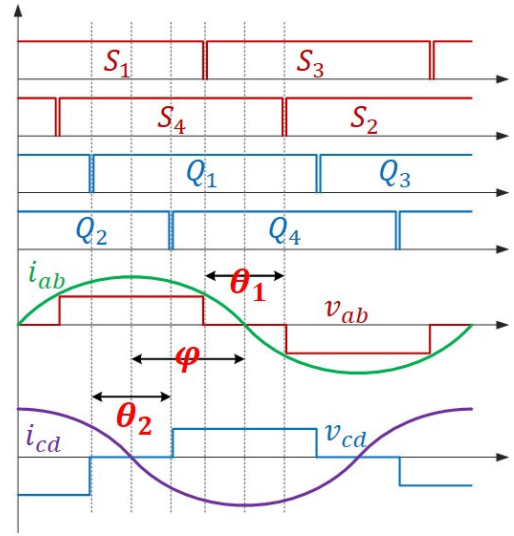


Fig. 2. Typical waveform of a classical LCC-LCC system.

The classical system is a high-order resonant converter based on DABs. Similar to the DAB PWM converters, there are three phases serving as the control variables. As shown in Fig. 2, the gate signal of TX bridge (S_1 – S_4) is given, which leads to a typical three-level voltage source v_{ab} for the resonant tank. θ_1 is the phase between S_1 – S_3 leg and S_2 – S_4 leg. Similarly, the RX bridge would offer a voltage source v_{cd} , where θ_2 is the phase between Q_1 – Q_3 leg and Q_2 – Q_4 leg. The phase difference between v_{ab} and v_{cd} is φ . The bridge output currents i_{ab} and i_{cd} are defined in Fig. 1. i_{tx} and i_{rx} represent the coil currents.

In the frequency domain, v_{ab} is represented by its phasor form \mathbf{V}_{ab} , whose amplitude is V_{ab} . All the other state variables would follow the same symbol format. When the phase of \mathbf{V}_{ab} is used as the reference (i.e., $\mathbf{V}_{ab} = V_{ab} \angle 0$), it has

$$V_{ab} = \int_0^{T_s} \sin \omega t \cdot v_{ab}(t) dt = \frac{4}{\pi} V_{in} \cos \frac{\theta_1}{2}. \quad (2)$$

For both the TX and RX sides, two state equations are given as

$$\begin{aligned} \mathbf{V}_{ab} &= j\omega L_t \mathbf{I}_{ab} + \frac{1}{j\omega C_t} (\mathbf{I}_{ab} - \mathbf{I}_{rx}) \\ -j\omega M \mathbf{I}_{tx} &= \left(j\omega L_{rx} + \frac{1}{j\omega C_{rx}} \right) \mathbf{I}_{rx} - \frac{1}{j\omega C_r} (\mathbf{I}_{cd} - \mathbf{I}_{rx}). \end{aligned} \quad (3)$$

At the resonance condition, \mathbf{I}_{tx} and \mathbf{I}_{cd} are solved as

$$\begin{aligned} \mathbf{I}_{tx} &= \frac{1}{j\omega L_t} \mathbf{V}_{ab} = \frac{4}{\pi} \frac{1}{\omega L_t} V_{in} \cos \frac{\theta_1}{2} \angle -\frac{\pi}{2} \\ \mathbf{I}_{cd} &= \frac{M}{\omega L_t L_r} \mathbf{V}_{ab} \angle \frac{\pi}{2} = \frac{4}{\pi} \frac{M}{\omega L_t L_r} V_{in} \cos \frac{\theta_1}{2} \angle \frac{\pi}{2}. \end{aligned} \quad (4)$$

It is clear that \mathbf{I}_{tx} and \mathbf{I}_{cd} are clamped by \mathbf{V}_{ab} . Due to the symmetry, similar clamping also exists for \mathbf{V}_{cd} , \mathbf{I}_{rx} , and \mathbf{I}_{ab} . When \mathbf{V}_{ab} serves as the reference, the phase of \mathbf{V}_{cd} is φ , and it has

$$\mathbf{V}_{cd} = \frac{4}{\pi} V_o \cos \frac{\theta_2}{2} \angle -\varphi. \quad (5)$$

TABLE I
PARAMETERS OF AN EXAMPLE SYSTEM

Symbol	Value	Symbol	Value	Symbol	Value
$L_{tx} & L_{rx}$	175 μH	$r_{tx} & r_{rx}$	0.40 Ω	$C_{tx} & C_{rx}$	19 nF
$L_t & L_r$	42 μH	$r_t & r_r$	0.08 Ω	$C_t & C_r$	60 nF
$V_{in} & V_o$	80 V	f_0	100 kHz	k	0.32

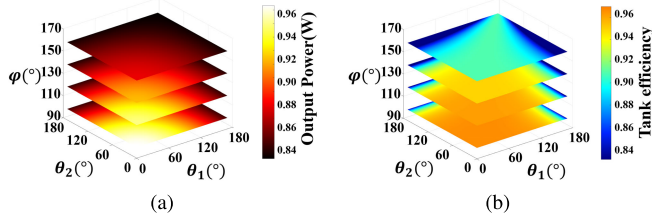


Fig. 3. Output power and tank efficiency under different θ_1 , θ_2 , and φ . (a) P_o . (b) η_{ac} .

Similar to (2)–(4), \mathbf{I}_{rx} and \mathbf{I}_{ab} are solved as

$$\begin{aligned} \mathbf{I}_{rx} &= \frac{4}{\pi} \frac{1}{\omega L_r} V_o \cos \frac{\theta_2}{2} \angle \left(-\frac{\pi}{2} - \varphi \right) \\ \mathbf{I}_{ab} &= \frac{4}{\pi} \frac{M}{\omega L_t L_r} V_o \cos \frac{\theta_2}{2} \angle \left(\frac{\pi}{2} - \varphi \right). \end{aligned} \quad (6)$$

B. Conflict Between ZVS and Tank Efficiency

Assume the coil equivalent series resistors (ESRs) of L_{tx} , L_{rx} , L_t , and L_r are r_{tx} , r_{rx} , r_t , and r_r , respectively. The loss of the coupler P_{coil} is

$$\begin{aligned} P_{coil} &= I_{tx}^2 r_{tx} + I_{rx}^2 r_{rx} \\ &= \frac{8}{\pi^2 \omega^2} \left[\left(\frac{V_{in}}{L_t} \right)^2 r_{tx} \cos^2 \frac{\theta_1}{2} + \left(\frac{V_o}{L_r} \right)^2 r_{rx} \cos^2 \frac{\theta_2}{2} \right]. \end{aligned} \quad (7)$$

The loss of the compensation inductor is

$$\begin{aligned} P_{comp} &= I_{ab}^2 r_t + I_{cd}^2 r_r \\ &= \frac{8}{\pi^2 \omega^2} \left[\left(\frac{M V_o}{L_t L_r} \right)^2 r_t \cos^2 \frac{\theta_2}{2} + \left(\frac{M V_{in}}{L_t L_r} \right)^2 r_r \cos^2 \frac{\theta_1}{2} \right]. \end{aligned} \quad (8)$$

The output power is

$$P_o = V_{cd} I_{cd} = \frac{8}{\pi^2} \frac{M}{\omega L_t L_r} V_{in} V_o \cos \frac{\theta_1}{2} \cos \frac{\theta_2}{2} \cos \left(\varphi - \frac{\pi}{2} \right). \quad (9)$$

For better illustration, an example system is given in Table I. According to (9), Fig. 3(a) shows the influence of the phase on the output power. The forward power transfer (i.e., $P_o > 0$) would request $\varphi \in [0, \pi]$. It is clear that $\varphi = (\pi/2)$ would maximize the output power for any given V_{in} , V_o , θ_1 , and θ_2 .

Given the loss and output power, the efficiency of the resonant tank is

$$\begin{aligned} \eta_{ac} &= \frac{P_o}{P_{coil} + P_{comp} + P_o} \\ &= \frac{c \cos \left(\varphi - \frac{\pi}{2} \right)}{a \frac{\cos \frac{\theta_1}{2}}{\cos \frac{\theta_2}{2}} + b \frac{\cos \frac{\theta_2}{2}}{\cos \frac{\theta_1}{2}} + c \cos \left(\varphi - \frac{\pi}{2} \right)} \end{aligned} \quad (10)$$

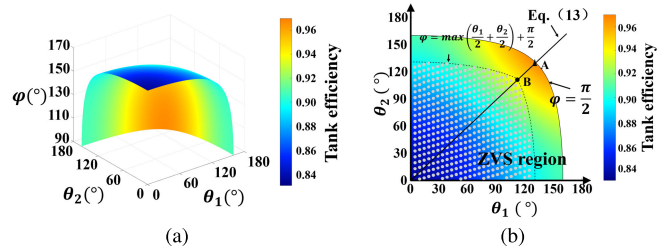


Fig. 4. Tank efficiency for a target output power. (a) Three-dimensional view. (b) Two-dimensional view.

where the intermediate parameters a , b , and c are

$$\begin{aligned} a &= \frac{8}{\pi^2 \omega^2} \left[\left(\frac{V_{in}}{L_t} \right)^2 r_{tx} + \left(\frac{M V_{in}}{L_t L_r} \right)^2 r_r \right] \\ b &= \frac{8}{\pi^2 \omega^2} \left[\left(\frac{V_o}{L_r} \right)^2 r_{rx} + \left(\frac{M V_o}{L_t L_r} \right)^2 r_t \right] \\ c &= \frac{8}{\pi^2} \frac{M}{\omega L_t L_r} V_{in} V_o. \end{aligned} \quad (11)$$

By taking the derivative with respect to $\cos(\varphi - (\pi/2))$, it has

$$\frac{\partial \eta_{ac}}{\partial \cos \left(\varphi - \frac{\pi}{2} \right)} > 0. \quad (12)$$

It means η_{ac} is proportional to $\cos(\varphi - (\pi/2))$, and $\varphi = (\pi/2)$ would lead to a maximum efficiency. This conclusion is justified in Fig. 3(b) when the parameters of Table I are used.

In a classical DAB-based PWM converter, TPS modulation is attractive for power regulation and efficiency enhancement. A common challenge is to fully explore the control freedoms of the active bridges (i.e., θ_1 , θ_2 , and φ) without losing ZVS operation. This logic is still valid when the DAB is applied to a high-order resonant converter. For a target output power (i.e., 100 W), (9) would offer an equality constrain for the control variables (i.e., θ_1 , θ_2 , and φ). According to (10), the efficiency map is shown in Fig. 4(a), which could be viewed as a curved surface of Fig. 3(b) by adding the power constrain. It still shows $\varphi = (\pi/2)$ helps maximize the efficiency.

Unlike φ , the influence of θ_1 and θ_2 is not straightforward in (10). A new term is defined in (10), i.e., $\beta = \cos(\theta_1/2)/\cos(\theta_2/2)$. By taking the derivative of η_{ac} with respect to β , i.e., $(\partial \eta_{ac} / \partial \beta) = 0$, it gives

$$\beta = \frac{\cos \frac{\theta_1}{2}}{\cos \frac{\theta_2}{2}} = \sqrt{\frac{(V_o L_r)^2 r_{rx} + (M V_o)^2 r_t}{(V_{in} L_t)^2 r_{tx} + (M V_{in})^2 r_r}}. \quad (13)$$

It means θ_1 and θ_2 are closely coupled when the efficiency is maximized. For a symmetrical system, $\theta_1 = \theta_2$. To explain this effect, a 2-D Fig. 4(b) is plotted based on Fig. 4(a), i.e., the projection of Fig. 4(a) on the bottom θ_1 - θ_2 plane. A straight solid line is actually defined by (13). The curve boundary means $\varphi = (\pi/2)$. When both the black lines meet at point A, a global maximum efficiency is achieved for the resonant tank.

The above conclusion shows the efficiency maximization needs to ensure $\varphi = (\pi/2)$ and (13). However, θ_1 and θ_2 cannot be freely tuned in a practical system when considering the requirements of active bridges. In [24], the ZVS operation for

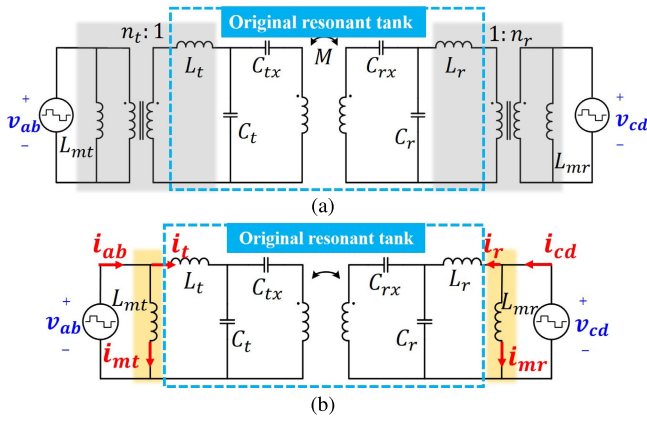


Fig. 5. Modified LCC compensation. (a) Original circuit model. (b) Equivalent circuit model when $n_t = n_r = 1$.

the LCC compensated system has been in-depth studied, and it requests the system to meet the constrain below

$$\varphi \geq \max\left(\frac{\theta_1}{2}, \frac{\theta_2}{2}\right) + \frac{\pi}{2}. \quad (14)$$

This inequality constrain actually defines a dot area in Fig. 4(b). Considering the limited ZVS region, the maximum efficiency point is B for a practical system. At this point, (13) is still fulfilled but $\varphi \neq (\pi/2)$. From the overall perspective, it means the elimination of the turn-on switching loss needs to sacrifice the conduction losses of the resonant tank. There naturally exists a conflict between the ZVS and tank efficiency. Since the efficiency, power, and ZVS requirements are all affected by the three phases, this article needs to minimize the conflict of the above objectives under TPS modulation.

III. MODIFIED LCC COMPENSATION

A. Circuit Model and Characteristics

To avoid the conflict of the classical LCC compensation, a modified compensation is proposed in Fig. 5(a). At the TX side, the input inductor L_t of Fig. 1 is replaced by a loosely coupled transformer, i.e., the gray part, where L_{mt} , L_t , and n_t represent the magnetic inductance, leakage inductance, and the turn ratio of the TX transformer, respectively. The RX compensation is modified in the same way. Similar technique has been introduced for the CPT system to boost the excitation voltage [26]. The major difference in this article is the function of the transformer, which is able to extend the ZVS range under TPS modulation. Besides, such a modification will not increase the number of magnetic components, because the additional transformer would adopt planar structure and then can be integrated with the coil. The magnetic design and integration will be discussed in Section IV, and here would focus on the steady-state characteristics of the modified system.

In Fig. 5(a), a nonunity turn ratio could adjust the voltage gain from the dc terminals to tank terminals. Besides, when the dc terminal voltage is different, the turn ratio could be designed to ensure the original tank has the same ac terminal voltage, i.e., the blue part. In a symmetrical IPT system, $n_t = n_r = 1$ would benefit the analysis and simplify the tank

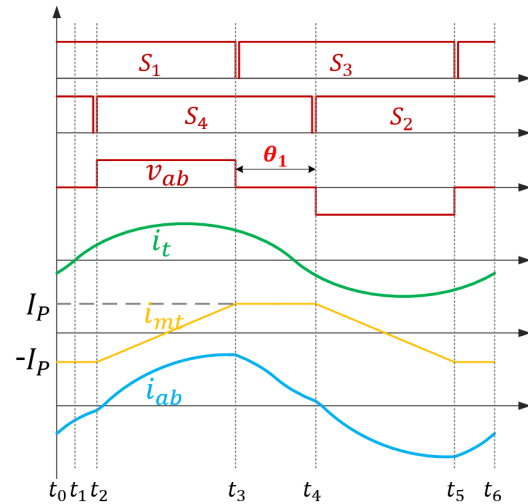


Fig. 6. Typical waveform of a modified system.

model as shown in Fig. 5(b). From the circuit perspective, two more shunt inductors (L_{mt} and L_{mr}) are added to the bridge ac ports. It is well-known that a shunt inductor is able to use the circulation energy for ZVS operation. Due to the parallel connection of the additional inductor, such a modification will not affect the steady-state characteristics of the original resonant tank. It means the state variables within the blue dot block could still be analyzed like Section II. The shunt inductor only affects the bridge output current.

The typical waveforms of the modified system are shown in Fig. 6. The energy is stored in the shunt inductor when V_{ab} is high. The stored energy would help discharge the transistor junction capacitors during the turn-on transition. For the TX side, L_{mt} is charged by a constant voltage from t_2 to t_3 . Therefore, the peak current of L_{mt} is easily derived as

$$I_p = \frac{(\pi - \theta_1)}{4\pi f} \frac{V_{in}}{L_{mt}}. \quad (15)$$

It is clear that I_p determines the current during the turn-on transition. A large I_p would benefit the ZVS operation.

In Fig. 6, the waveform of v_{ab} and i_{ab} actually reflects the ZVS operation of the TX bridge. At t_3 and t_5 instance, both S_1 and S_3 are turned on and ZVS can be ensured. Note that both S_2 and S_4 are turned off right before the turn on of S_1 and S_3 . There is no ZVS lost issue for S_1 – S_3 leg. However, at t_2 and t_4 instance, an uncertain i_{ab} would cause ZVS lost for S_2 – S_4 leg. Taking instance t_2 as an example, a negative i_{ab} is necessary for S_4 , which means

$$i_{ab}(t_2) = i_t(t_2) + i_{mt}(t_2) < 0. \quad (16)$$

At t_2 , $i_{mt}(t_2)$ equals $-I_p$, and $i_t(t_2)$ should be calculated based on its time-domain equation. Since i_t of the modified compensation is exactly the same as i_{ab} of the original compensation, (6) would be used to derive $i_t(t)$ as below

$$i_t(t) = \frac{4}{\pi} \frac{M}{\omega L_t L_r} V_o \cos \frac{\theta_2}{2} \sin\left(\omega t + \frac{\pi}{2} - \varphi\right). \quad (17)$$

Since $\omega t_2 = (\theta_1/2)$, taking (15) and (17) into (16), it would give

$$L_{mt} < \frac{L_t L_r V_{in} (\pi - \theta_1)}{2V_o M \sin(\frac{\theta_1}{2} + \frac{\pi}{2} - \varphi) \cos \frac{\theta_2}{2}}. \quad (18)$$

Similarly, for the RX side, it also has

$$L_{mr} < \frac{L_r L_r V_o (\pi - \theta_2)}{2V_{in} M \sin(\frac{\theta_2}{2} + \frac{\pi}{2} - \varphi) \cos \frac{\theta_1}{2}}. \quad (19)$$

The above two inequality constrains actually define the necessary condition for the ZVS operation. When M varied in practice, the shunt inductance design should consider the maximum coupling as the worst case.

B. Efficiency Enhancement

Although the modified compensation is helpful to extend the ZVS range, the additional shunt inductor would also cause additional conduction losses. Assume the ESR of L_{mt} and L_{mr} is r_{mt} and r_{mr} , the additional conduction loss caused by r_{mt} is (under fundamental approximation)

$$I_{mt} = \frac{2}{T_s} \int_0^{T_s} i_{mt}(t) \cos \omega t dt = \frac{2T_s}{\pi^2} \frac{V_{in}}{L_{mt}} \cos \frac{\theta_1}{2}$$

$$P_{mt} = I_{mt}^2 r_{mt} = \left(\frac{2T_s}{\pi^2} \frac{V_{in}}{L_{mt}} \right)^2 r_{mt} \cos^2 \frac{\theta_1}{2}. \quad (20)$$

The loss caused by r_{mt} is

$$P_{mr} = \left(\frac{2T_s}{\pi^2} \frac{V_{in}}{L_{mr}} \right)^2 r_{mr} \cos^2 \frac{\theta_1}{2}. \quad (21)$$

The overall loss of the resonant tank becomes

$$P'_{\text{loss}} = P_{\text{coil}} + P_{\text{comp}} + P_{mt} + P_{mr} \quad (22)$$

where P_{coil} and P_{comp} are given in (7) and (8). The efficiency of the new tank is derived as

$$\eta'_{\text{ac}} = \frac{P_o}{P'_{\text{loss}} + P_o}$$

$$= \frac{c \cos(\varphi - \frac{\pi}{2})}{a' \frac{\cos \frac{\theta_1}{2}}{\cos \frac{\theta_2}{2}} + b' \frac{\cos \frac{\theta_2}{2}}{\cos \frac{\theta_1}{2}} + c' \cos(\varphi - \frac{\pi}{2})} \quad (23)$$

where

$$a' = \frac{8}{\pi^2 \omega^2} \left[\left(\frac{V_{in}}{L_t} \right)^2 r_{tx} + \left(\frac{M V_{in}}{L_t L_r} \right)^2 r_r \right] + \left(\frac{1}{2\omega L_{mt}} V_{in} \right)^2 r_{mt}$$

$$b' = \frac{8}{\pi^2 \omega^2} \left[\left(\frac{V_o}{L_r} \right)^2 r_{rx} + \left(\frac{M V_o}{L_t L_r} \right)^2 r_t \right] + \left(\frac{1}{2\omega L_{mr}} V_o \right)^2 r_{mr}$$

$$c' = c = \frac{8}{\pi^2} \frac{M}{\omega L_t L_r} V_{in} V_o. \quad (24)$$

This uniform efficiency expression is helpful to compare the performance of the original system and the modified one.

Based on Table I, the influence of L_{mt} ($=L_{mr}$) is discussed in Fig. 7. The original system means an infinite L_{mt} . By decreasing L_{mt} , the ZVS region (enclosed by the dot curve) would gradually increase, which means the operation point would be closer to Point A. The modified system actually enhances the tank efficiency by slightly increasing

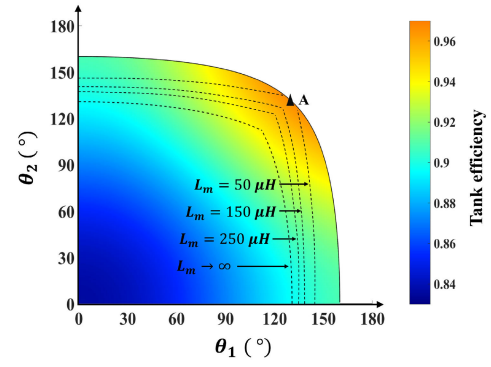


Fig. 7. Two-dimensional efficiency map of the modified system.

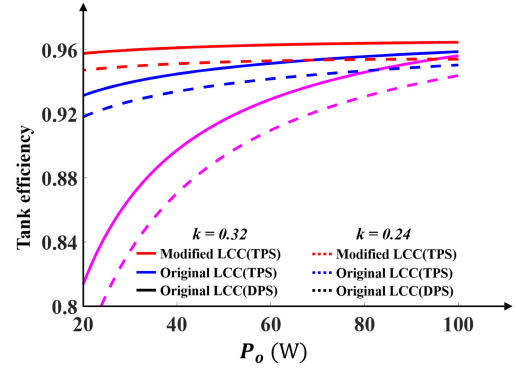


Fig. 8. Tank efficiency comparison for different P_o (full load: 100 W) and different coupling coefficients k .

the conduction loss of shunt inductance. Note that the ESR of the magnetic inductance is usually very limited. To justify the efficiency improvement, two systems are compared in simulation. For the new system, all the circuit parameters still follow Table I. The shunt inductance and its ESR are $L_{mt} = L_{mr} = 70 \mu\text{H}$ and $r_{mt} = r_{ms} = 0.12 \Omega$. In Fig. 8, the application of DPS modulation in the original LCC system negatively impacts the light load efficiency due to limited control freedoms. However, with the implementation of TPS, the efficiency undergoes a significant improvement. Moreover, using modified LCC compensation, the tank efficiency experiences further enhancement when combined with TPS modulation. This demonstrates that the new system maintains high efficiency across a broad load range, particularly in light load conditions. Importantly, these conclusions remain valid even when there are variations in coupling.

IV. MAGNETIC INTEGRATION

A. Magnetic Structure and Model

The modified system needs two magnetic components for the TX compensation, i.e., L_{mt} and L_t in Fig. 5(a). These two components would be offered by a single planar TX transformer. The proposed coupler with integrated compensation transformer is shown in Fig. 9(a). This configuration aids in containing the flux within the coupling area, thereby reducing leakage. Each side consists of four layers: a coil layer, two magnetic layers, and a transformer winding layer. Each side of Fig. 9(a) actually consists of two functional parts. Inside the blue block, it is a typical coupler. The transformer is built by magnetic within the black box. The transformer and coil

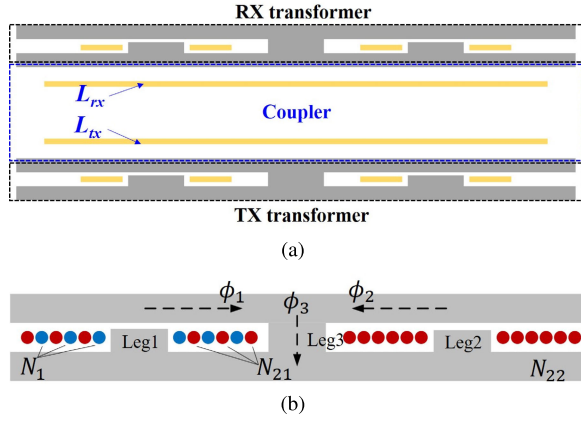


Fig. 9. Magnetic integration. (a) Whole structure. (b) Transformer structure.

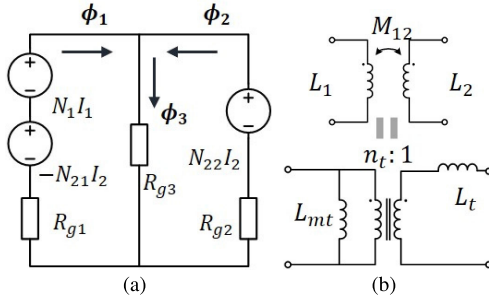


Fig. 10. Transformer model. (a) Magnetic model. (b) Circuit model.

would use the middle magnetic layer, with the coil-induced flux primarily flowing through the shared layer toward the edges. This separation effectively decouples the coil from the transformer. Consequently, the coil design would still adhere to the conventional approach.

The structure of the TX transformer is zoomed in Fig. 9(b). The objective is to design the transformer size parameters to meet the circuit requirement, i.e., L_t , n_t , and L_{mt} . Based on the analysis in Section III, the modified compensation method eliminates the need for an ideal transformer. Instead, a loosely coupled transformer is required to provide the necessary inductances, L_t , n_t , and L_{mt} . As a result, the proposed transformer adopts an interleaved winding structure, as illustrated in Fig. 9(b). The red winding is connected to C_t , while the blue winding is connected to the inverter. In the red winding, the majority of the turns are wound around Leg 2, denoted as N_{22} . The remaining portion of the winding is interleaved and wound around Leg 1, with a turn count of N_{21} . In contrast, all the windings of the blue winding are wound around Leg 1, with a turn count of N_1 . Both Leg 1 and Leg 2 have fixed air gaps. The turn counts (N_1 , N_{21} , and N_{22}) serve as the design variables in this configuration.

Fig. 10(a) shows the equivalent magnetic circuit model of Fig. 9(b). R_{g1} , R_{g2} , and R_{g3} represent the reluctance of the flux paths, which are determined by the magnetic structure. The magnetic flux of each branch could be solved by

$$\begin{aligned} \phi_1 R_{g1} + \phi_3 R_{g3} &= N_1 I_1 - N_{21} I_2 \\ -\phi_3 R_{g3} + \phi_2 R_{g2} &= N_{22} I_2 \\ \phi_1 + \phi_2 - \phi_3 &= 0. \end{aligned} \quad (25)$$

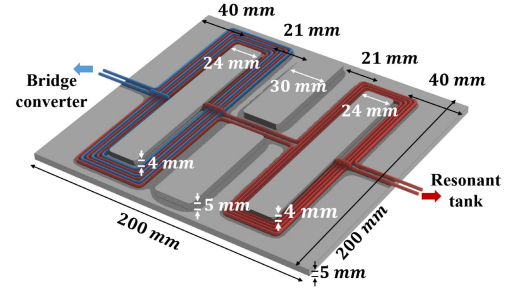


Fig. 11. Maxwell simulation setup.

When the magnetic components are modeled as two coupled inductors, the self inductance and mutual inductance are determined by the flux as

$$\begin{aligned} L_1 &= \frac{N_1 \phi_1}{I_1} \Big|_{I_2=0} \\ L_2 &= \frac{N_{21} \phi_1 - N_{22} \phi_2}{I_2} \Big|_{I_1=0} \\ M_{12} &= \frac{N_1 \phi_1}{I_2} \Big|_{I_1=0}. \end{aligned} \quad (26)$$

Taking the solution of (25) into the above definition, the proposed symmetrical structure ($R_{g3} \ll R_{g1} = R_{g2}$) has $L_1 = N_1^2/R_{g1}$, $L_2 = (N_{21}^2 + N_{22}^2)R_{g1}$, and $M_{12} = -N_1 N_{21}/R_{g1}$.

According to the equivalent circuit theory, the coupled inductor model can be transformed into a transformer model, as illustrated in Fig. 10(b). Finally, it has

$$\begin{aligned} L_{mt} &= L_1 = N_1^2/R_{g1} \\ L_t &= L_2 - M^2/L_1 = N_{22}^2/R_{g1} \\ n_t &= L_1/M_{12} = N_1/N_{21}. \end{aligned} \quad (27)$$

It demonstrates that the turn count plays a crucial role in establishing the necessary circuit parameters.

B. Simulation-Based Transformer Design

In the magnetic model, the calculated turn number needs to be a post validation through a simulation tool, like Maxwell. The TX transformer structure is shown in Fig. 11 (removing the cover plate), which is like a planar E core. This figure shows the layout and size information. The bottom layer is a square plate (200-mm length) and its thickness is 5 mm. The height of Leg 1–Leg 3 is 4, 4, and 5 mm respectively.

This article demonstrates a symmetrical IPT system, which means $L_t = L_r$, $L_{mt} = L_{mr}$, and $n_t = n_r$. According to (4), the output current I_{cd} is clamped by the input voltage V_{ab} , and the conversion ratio is inversely proportional to L_t and L_r . It means L_t and L_r actually determine the output current for a given M . Since $n_t = n_r$, this turn ratio will not affect the overall conversion gain, and a unity turn ratio is used for convenience. The major design constrain is L_{mt} . Based on the above design consideration, a Maxwell simulation is used to extract the transformer circuit parameters for different N_1 and N_{22} .

Fig. 12 shows the influence of N_1 and N_{22} on L_t and L_{mt} . It is clear that L_t is mainly determined by N_{22} and L_{mt} is mainly determined by N_1 . These results are consistent with the

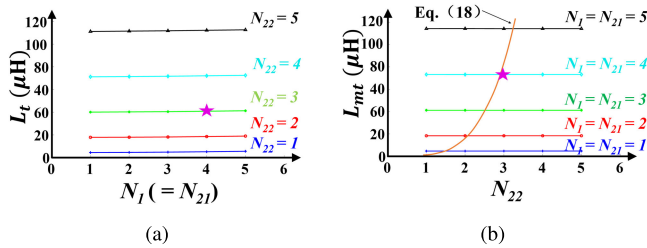


Fig. 12. Sweeping N_1 and N_{22} . (a) L_t . (b) L_{mt} .

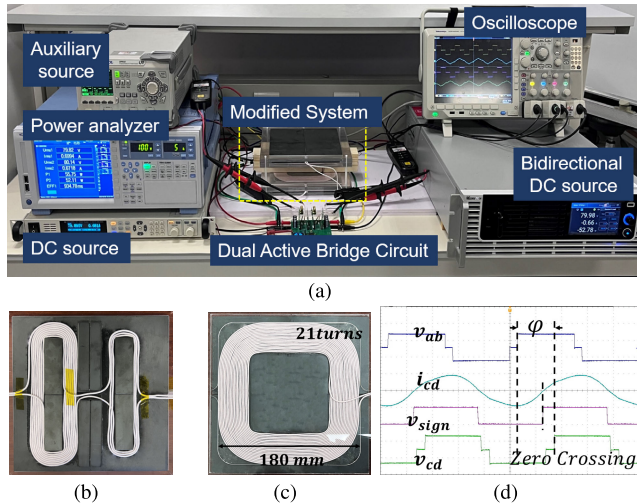


Fig. 13. Experiment. (a) Test platform. (b) Transformer side (removing the covering plate). (c) Coil side. (d) TPS modulation with ZCD circuits.

model-based analysis in (27). According to (18), the up limit of L_{mt} is affected by L_t ($=L_r$). Therefore, when sweeping N_1 and N_{22} , each L_t would define a up limit for L_{mt} by the orange curve of Fig. 12(b). Finally, the transformer is designed at the star point, where $N_1 = N_{21} = 4$ and $N_{22} = 3$. The magnetic model enables quantitative prediction of the simulation results. Once the magnetic component is designed, field simulations can be used to analyze winding and core losses. This analysis allows for the derivation of the corresponding ESR for loss analysis.

The original compensation method requires two separate input inductors, whereas the modified method integrates them into the existing planar coupler. This planar structure offers advantages for the charging of moving robots. By manipulating three circuit parameters (L_{mt} , L_t , and n_t), it is possible to design the voltage gain, the ZVS region, and the voltage and current ratings of the resonant components. It is worth noting that this modification is applicable to other IPT and capacitive power transfer systems as well.

V. EXPERIMENT VERIFICATION

The final experiment setup is shown in Fig. 13(a). A symmetrical IPT system is built with DABs. A dc power supply is used to drive the whole system, and the bidirectional dc source is used to mimic the battery. The compensation inductors are integrated with the coupler as shown in Fig. 13(b) and (c). The detailed size parameters of the magnetic structure are given in Fig. 11, which is built by standard magnetic sheets. The magnetic core material is TDK PC40. At 100 kHz,

TABLE II
REAL-SYSTEM PARAMETERS

Symbol	Value	Symbol	Value	Symbol	Value
f_0	100 kHz	L_t	43.8 μH	L_r	41.5 μH
V_{in}, V_o	80 V	C_t	57.8 nF	C_r	61.0 nF
Distance	100 mm	L_{tx}	174.5 μH	L_{rx}	175.2 μH
k	[0.24 0.32]	C_{tx}	19.4 nF	C_{rx}	19.0 nF
Power	100 W	r_{tx}	0.41 Ω	r_{rx}	0.42 Ω
Switch	GS61004B	L_{mt}	71.3 μH	L_{mr}	71.5 μH
Magnetic	PC 40	r_{mt}	0.12 Ω	r_{mr}	0.12 Ω

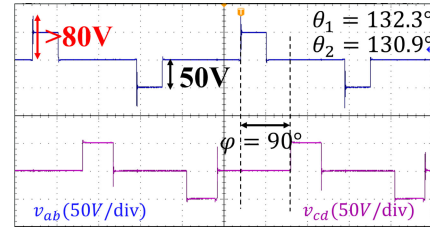


Fig. 14. AC terminal voltage of the original system without considering ZVS requirements.

the equivalent circuit parameters of the magnetic components are measured by the impedance analyzer, and then the compensation capacitance is designed according to (1). All the real parameters are shown in Table II. The coupling coefficient between the coil and the transformer is 0.005. In the TPS modulation, the RX-side controller needs to adjust the phase difference between the TX and the RX. The famous zero-current detection (ZCD) would be used. As shown in Fig. 13(d), the inverter output voltage (v_{ab}) is controlled by the TX driving signal, and this voltage would clamp the rectifier output current (i_{cd}). The ZCD circuit would detect the crossing zero point and give it for RX to drive the RX bridge. When the TPS modulation of the original system does not consider the ZVS demands, it would keep ϕ at 90° and adjust θ_1 ($=\theta_2$) to meet power demand. The waveform is shown in Fig. 14, where the switching voltage ringing is significant and the power level is limited to avoid breaking the transistor.

Fig. 15(a)–(c) shows the steady-state waveforms of the modified system under different loading conditions. All the phase information is given. The waveform of the original system is shown in Fig. 15(d)–(f). For all the six figures, it would have $\theta_1 \approx \theta_2$, which justified the derivation of (13). Under the same load condition, it is clear that ϕ is much closer to the ideal value ($\pi/2$) for the modified system, which means $\phi \leq (\theta_1/2) + (\pi/2)$. For the original system, it almost has $\phi = (\theta_1/2) + (\pi/2)$. It means existence of L_{mt} and L_{mr} would help enlarge the ZVS region under TPS modulation. In this article, the design of L_{mt} and L_{mr} does not mean the ZVS region needs to fully enclose Point A in Fig. 7. On one side, the inductance is determined by the turn number and cannot be continuously tuned. On the other side, a heavy load condition would use the resonant tank current for ZVS operation, and the addition of shunt inductance would not benefit this situation. Actually, L_{mt} and L_{mr} offer a design freedom to modify the efficiency curve shape.

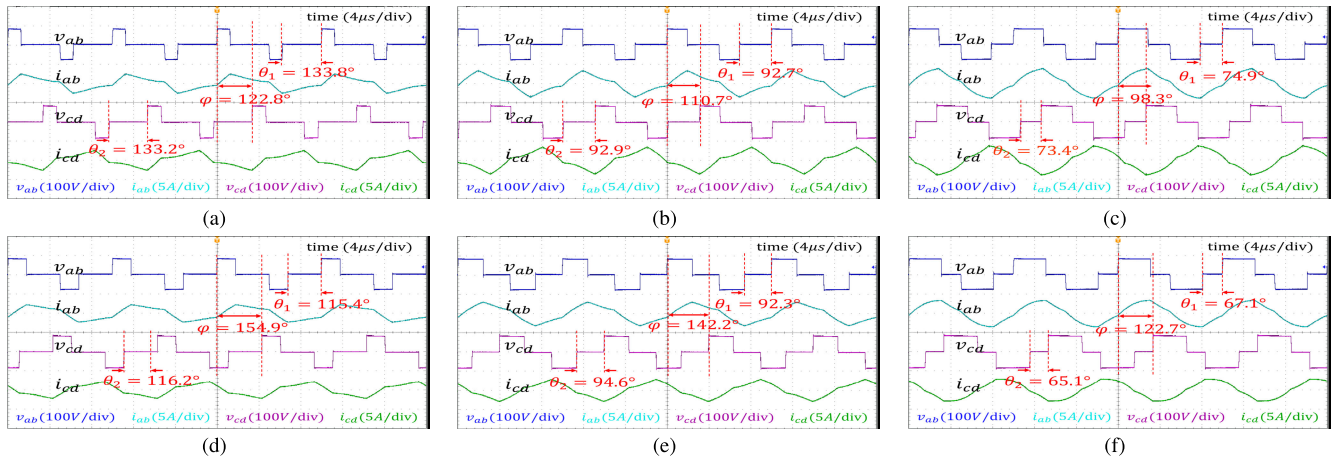


Fig. 15. Steady-state waveform of the dual bridges. (a) Modified system: 20% load. (b) Modified system: 50% load. (c) Modified system: 100% load. (d) Original system: 20% load. (e) Original system: 50% load. (f) Original system: 100% load.

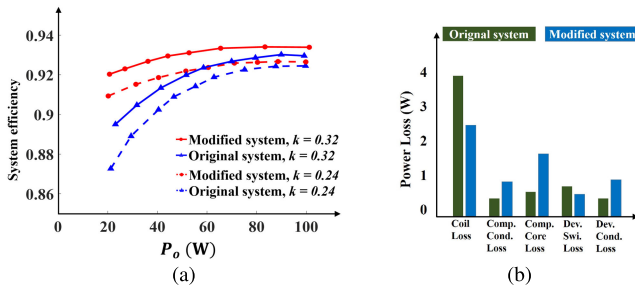


Fig. 16. Efficiency and loss comparison. (a) Measured dc efficiency comparison with various P_o and k . (b) Loss breakdown of full-load condition.

Fig. 16 shows comparison of the efficiency of the modified system and the original one under TPS modulation. Although the measured dc efficiency is lower than the calculated ac efficiency of Fig. 8 due to the losses of bridges, the basic dc characteristics are almost the same as the ac ones. When $k = 0.32$, it shows the efficiency of the modified system is higher than 92.0% for a wide load range. The efficiency improvement (1.9%) is more obvious at light load condition. When misalignment happens ($k = 0.24$), the efficiency improvement (about 3.7%) at light load becomes more significant. At the full-load condition, the efficiency of the modified system is slightly improved. To explain this result, it needs to review the conflict of ZVS operation and tank efficiency. For any system, a heavier load usually means a higher tank current, which actually benefits ZVS. Therefore, at full-load condition, the conflict between ZVS operation and tank efficiency is not significant for the original system. As shown in Fig. 15(f), the value of φ actually reflects this conflict. Compared with the light load, φ of the full-load condition is much closer to $\pi/2$. The modified system would have a higher conduction loss due to the additional shunt inductance. A detailed loss breakdown is compared in Fig. 16(b). As a result, the modified compensation would have a better efficiency for a wide load, especially for the light load.

VI. CONCLUSION

This article develops a modified LCC compensation and a magnetic integration solution for IPT. It discusses the basic operation of the system using original LCC compensation and shows the limitation of TPS modulation for efficiency

maximization when meeting the ZVS demands. By replacing the compensation inductor by a loosely coupled transformer, the additional shunt magnetic inductor would benefit the ZVS operation and the leakage inductance would act as the original compensation inductor. Such a modification will not affect the operation of the resonant tank. Besides, the transformer is able to be integrated with the coupler to form a compact and low-profile design. Through winding interleaving, the magnetic model is used to design the transformer parameters. The final system has a peak efficiency of 93.4% and would maintain the efficiency above 91.0% for a wide load and coupling condition.

REFERENCES

- [1] W. Liu, K. T. Chau, C. H. T. Lee, C. Jiang, W. Han, and W. H. Lam, "A wireless dimmable lighting system using variable-power variable-frequency control," *IEEE Trans. Ind. Electron.*, vol. 67, no. 10, pp. 8392–8404, Oct. 2020.
- [2] P. Machura, V. De Santis, and Q. Li, "Driving range of electric vehicles charged by wireless power transfer," *IEEE Trans. Veh. Technol.*, vol. 69, no. 6, pp. 5968–5982, Jun. 2020.
- [3] B. Zhang, R. B. Carlson, J. G. Smart, E. J. Dufek, and B. Liaw, "Challenges of future high power wireless power transfer for light-duty electric vehicles—technology and risk management," *eTransportation*, vol. 2, Nov. 2019, Art. no. 100012.
- [4] S. Jayalath and A. Khan, "Design, challenges, and trends of inductive power transfer couplers for electric vehicles: A review," *IEEE J. Emerg. Sel. Topics Power Electron.*, vol. 9, no. 5, pp. 6196–6218, Oct. 2021.
- [5] R. He, P. Zhao, G. Ning, K. Yue, Y. Liu, and M. Fu, "Optimal driving and loading scheme for multiple-receiver inductive power transfer," *IEEE Trans. Ind. Electron.*, vol. 69, no. 12, pp. 12665–12675, Dec. 2022.
- [6] M. Budhia, J. T. Boys, G. A. Covic, and C.-Y. Huang, "Development of a single-sided flux magnetic coupler for electric vehicle IPT charging systems," *IEEE Trans. Ind. Electron.*, vol. 60, no. 1, pp. 318–328, Jan. 2013.
- [7] S. Kim, G. A. Covic, and J. T. Boys, "Tripolar pad for inductive power transfer systems for EV charging," *IEEE Trans. Power Electron.*, vol. 32, no. 7, pp. 5045–5057, Jul. 2017.
- [8] A. Ahmad, M. S. Alam, and A. A. S. Mohamed, "Design and interoperability analysis of quadruple pad structure for electric vehicle wireless charging application," *IEEE Trans. Transport. Electrification*, vol. 5, no. 4, pp. 934–945, Dec. 2019.
- [9] C.-S. Wang, G. A. Covic, and O. H. Stielau, "Power transfer capability and bifurcation phenomena of loosely coupled inductive power transfer systems," *IEEE Trans. Ind. Electron.*, vol. 51, no. 1, pp. 148–157, Feb. 2004.
- [10] R. He, P. Zhao, M. Fu, Y. Liu, H. Wang, and J. Liang, "Decomposition and synthesis of high-order compensated inductive power transfer systems for improved output controllability," *IEEE Trans. Microw. Theory Techn.*, vol. 67, no. 11, pp. 4514–4523, Nov. 2019.

- [11] W. Zhang, S.-C. Wong, C. K. Tse, and Q. Chen, "Analysis and comparison of secondary series- and parallel-compensated inductive power transfer systems operating for optimal efficiency and load-independent voltage-transfer ratio," *IEEE Trans. Power Electron.*, vol. 29, no. 6, pp. 2979–2990, Jun. 2014.
- [12] P. Zhao, G. Zheng, R. He, Y. Liu, and M. Fu, "A 45-W two-stage wireless fast charger using unregulated inductive power transfer," *IEEE J. Emerg. Sel. Topics Ind. Electron.*, vol. 2, no. 3, pp. 287–296, Jul. 2021.
- [13] S. Li, W. Li, J. Deng, T. D. Nguyen, and C. C. Mi, "A double-sided LCC compensation network and its tuning method for wireless power transfer," *IEEE Trans. Veh. Technol.*, vol. 64, no. 6, pp. 2261–2273, Jun. 2015.
- [14] G. Zheng, P. Zhao, H. Li, and M. Fu, "Small-signal model of an inductive power transfer system using LCC–LCC compensation," *IEEE Trans. Ind. Appl.*, vol. 58, no. 1, pp. 1201–1210, Jan. 2022.
- [15] T. Kan, F. Lu, T.-D. Nguyen, P. P. Mercier, and C. C. Mi, "Integrated coil design for EV wireless charging systems using LCC compensation topology," *IEEE Trans. Power Electron.*, vol. 33, no. 11, pp. 9231–9241, Nov. 2018.
- [16] Y. Zhang, L. Wang, Y. Guo, and C. Tao, "Null-coupled magnetic integration for EV wireless power transfer system," *IEEE Trans. Transport. Electric.*, vol. 5, no. 4, pp. 968–976, Dec. 2019.
- [17] H. Li, K. Wang, J. Fang, and Y. Tang, "Pulse density modulated ZVS full-bridge converters for wireless power transfer systems," *IEEE Trans. Power Electron.*, vol. 34, no. 1, pp. 369–377, Jan. 2019.
- [18] Z. Hua, K. T. Chau, W. Liu, X. Tian, and H. Pang, "Autonomous pulse frequency modulation for wireless battery charging with zero-voltage switching," *IEEE Trans. Ind. Electron.*, vol. 70, no. 9, pp. 8959–8969, Sep. 2023.
- [19] Y. Zhang, S. Chen, X. Li, and Y. Tang, "Dual-side phase-shift control of wireless power transfer implemented on primary side based on driving windings," *IEEE Trans. Ind. Electron.*, vol. 68, no. 9, pp. 8999–9002, Sep. 2021.
- [20] U. K. Madawala and D. J. Thrimawithana, "A bidirectional inductive power interface for electric vehicles in V2G systems," *IEEE Trans. Ind. Electron.*, vol. 58, no. 10, pp. 4789–4796, Oct. 2011.
- [21] X. Zhang et al., "A control strategy for efficiency optimization and wide ZVS operation range in bidirectional inductive power transfer system," *IEEE Trans. Ind. Electron.*, vol. 66, no. 8, pp. 5958–5969, Aug. 2019.
- [22] S. Jia, C. Chen, P. Liu, and S. Duan, "A digital phase synchronization method for bidirectional inductive power transfer," *IEEE Trans. Ind. Electron.*, vol. 67, no. 8, pp. 6450–6460, Aug. 2020.
- [23] D. Zhang, M. Chen, B. Li, X. Wang, X. Sun, and F. Jiang, "Synchronization strategy based on resonant current detection for bidirectional wireless charging system," *IEEE Trans. Power Electron.*, vol. 37, no. 9, pp. 11436–11449, Sep. 2022.
- [24] Y. Liu, U. K. Madawala, R. Mai, and Z. He, "An optimal multivariable control strategy for inductive power transfer systems to improve efficiency," *IEEE Trans. Power Electron.*, vol. 35, no. 9, pp. 8998–9010, Sep. 2020.
- [25] K. N. Mude and K. Aditya, "Comprehensive review and analysis of two-element resonant compensation topologies for wireless inductive power transfer systems," *Chin. J. Electr. Eng.*, vol. 5, no. 2, pp. 14–31, Jun. 2019.
- [26] A. L. F. Stein, P. A. Kyaw, and C. R. Sullivan, "Wireless power transfer utilizing a high- Q self-resonant structure," *IEEE Trans. Power Electron.*, vol. 34, no. 7, pp. 6722–6735, Jul. 2019.



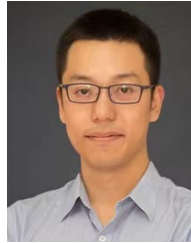
Xinlin Wang (Graduate Student Member, IEEE) received the B.S. degree in electrical engineering and automation from Hohai University, Nanjing, China, in June 2020. He is currently pursuing the master's degree in power electronics with the School of Information Science and Technology, ShanghaiTech University, Shanghai, China.

His research interests include multiple-coil IPT systems and bidirectional IPT systems.



Rong He (Graduate Student Member, IEEE) received the B.S. degree in electrical engineering and automation from the Harbin Institute of Technology, Weihai, China, in 2018. She is currently pursuing the Ph.D. degree in power electronics with the School of Information Science and Technology, ShanghaiTech University, Shanghai, China.

Her research interests include compensation of the IPT systems and multiple-coil IPT systems.



Haoyu Wang (Senior Member, IEEE) received the bachelor's degree (Hons.) in electrical engineering from Zhejiang University, Hangzhou, China, in 2009, and the Ph.D. degree in electrical engineering from the University of Maryland at College Park, College Park, MD, USA, in 2014.

In September 2014, he joined the School of Information Science and Technology, ShanghaiTech University, Shanghai, China, where he is currently a tenured Associate Professor. His research interests include power electronics, plug-in electric and hybrid electric vehicles, applications of wide bandgap semiconductors, renewable energy harvesting, and power management integrated circuits.

Dr. Wang is an Associate Editor of *IEEE TRANSACTIONS ON INDUSTRIAL ELECTRONICS*, *IEEE TRANSACTIONS ON TRANSPORTATION ELECTRIFICATION*, and *CPSS Transactions on Power Electronics and Applications*.

Dr. Wang is an Associate Editor of *IEEE TRANSACTIONS ON INDUSTRIAL ELECTRONICS*, *IEEE TRANSACTIONS ON TRANSPORTATION ELECTRIFICATION*, and *CPSS Transactions on Power Electronics and Applications*.



Junrui Liang (Senior Member, IEEE) received the B.E. and M.E. degrees in instrumentation engineering from Shanghai Jiao Tong University, Shanghai, China, in 2004 and 2007, respectively, and the Ph.D. degree in mechanical and automation engineering from The Chinese University Hong Kong, Hong Kong, SAR, China, in 2010.

He is currently an Associate Professor with the School of Information Science and Technology, ShanghaiTech University, Shanghai. His research interests include energy conversion and power conditioning circuits, kinetic energy harvesting and vibration suppression, the IoT devices, and mechatronics.

He was a recipient of three best paper awards in international conferences, such as the IEEE International Conference on Information and Automation, in 2009 and 2010, and the International Conferences on Vibration and Energy Harvesting Applications, in 2021. He is the General Chair of the Second International Conference on Vibration and Energy Harvesting Applications (VEH), in 2019. He is an Associate Editor of *IET Circuits, Devices and Systems*.



Minfan Fu (Senior Member, IEEE) received the B.S., M.S., and Ph.D. degrees in electrical and computer engineering from the University of Michigan–Shanghai Jiao Tong University Joint Institute, Shanghai Jiao Tong University, Shanghai, China, in 2010, 2013, and 2016, respectively.

From 2016 to 2018, he held a postdoctoral position with the Center for Power Electronics Systems (CPES), Virginia Polytechnic Institute and State University, Blacksburg, VA, USA. He is currently an Assistant Professor with the School of Information Science and Technology, ShanghaiTech University, Shanghai, China.

He holds one U.S. patent, 15 Chinese patents, and has authored or coauthored more than 100 papers in prestigious IEEE journals and conferences. His research interests include wireless power transfer, high-frequency power conversion, and application of wide bandgap devices.